Improving the TanDEM-X Water Mask by Exploiting the Acquisition Geometry

Paolo Valdo, German Aerospace Center (DLR), paolo.valdo@dlr.de, Germany
Francescopaolo Sica, German Aerospace Center (DLR), francescopaolo.sica@dlr.de, Germany
Paola Rizzoli, German Aerospace Center (DLR), paola.rizzoli@dlr.de, Germany

Abstract

In this paper we propose an enhancement of the TanDEM-X Water Mask Indicator (WAM). The proposed approach takes into account the geometric properties of SAR acquisition scenes, in order to precisely detect image areas affected by severe geometric distortions, namely Shadow and Layover. The presence of such effects can severely reduce the performance of the overall classification. In particular we concentrate upon the developed TanDEM-X WAM classification algorithm which shows misclassified areas in correspondence of high-relief terrain. The proposed approach aims at reducing this kind of misclassification errors, leading to an improvement of the TanDEM-X WAM performance. The impact of the input DEM accuracy is investigated as well, together with the potentials of modifying the detection algorithm itself. The long-term objective is to develop a reliable and efficient algorithm to provide high-resolution large-scale water masks from TanDEM-X interferometric data.

1 Introduction

The TerraSAR-X satellite was launched on June 15th 2007 and it was followed by its twin satellite TanDEM-X on 21st June 2010. Since then, they have been flying in a close orbit formation for the TanDEM-X mission, with the objective of generating a global Digital Elevation Model (DEM) over the entire Earth surface, which has been completed in 2016 [1].
The Global TanDEM-X DEM product has been provided with an additional information layer: the Water Indication Mask (WAM) as shown in [2], which indicates the Earth surface zones covered by water bodies (Seas, Lakes, Rivers, etc.), at a spatial resolution of 12 m.
The methodology used to generate the TanDEM-X WAM is mainly based on thresholding SAR amplitude and interferometric coherence. It is straightforward to understand that geometric distortion, affecting SAR backscattering and interferometric pair correlation, strongly influences the classification algorithm performance. Indeed, the TanDEM-X WAM, while showing great performance and a good degree of completeness in flat areas, it misclassifies regions where the orography is complex (e.g. mountainous areas).
In order to counteract the geometric distortion, the TanDEM-X WAM algorithm takes into account the Shadow and Layover maps generated by the ITP processor [3], that in some regions underestimate Shadow and Layover areas. An example is given in **Figure 1** where the ITP mask is compared with the expected Shadow regions obtained from the image geometry.
In the presented work, while retaining the classification algorithm, we investigate the potentiality of a more accurate Shadow and Layover detection together with additional filtering strategies. This work is meant as a starting point for the development of a more effective classification algorithm.
The paper shows, in section 2, the implemented approach for a reliable detection of shadow and layover areas. Then, in section 3, we describe the considered test site and input data. The analysis of the impact on the enhanced water mask (EWAM) of the input shadow and layover mask, the external reference DEM, and the threshold on the local slope, is discussed in section 4. Finally, conclusions and outlook are presented in section 5.

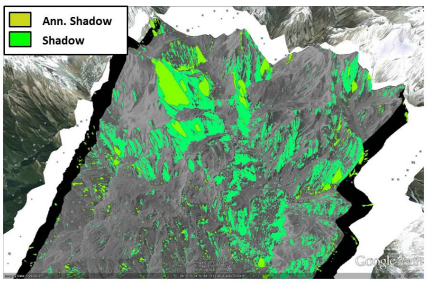

Figure 1: Annotated Shadow (light green) vs Real Shadow (dark green) in Himalaya. Annotated Shadow underestimates the real Shadow extension.

2 Shadow and Layover Detection

Shadow and Layover are two geometric distortions that are generated by a combination of terrain topography and side-looking geometry. They both take place in presence of sloping terrain whose inclination is higher than the radar looking angle.
In particular, with Shadow is normally indicated the absence of signal due to the presence of obstacles in the

radar line-of-sight direction. This phenomenon happens for decreasing terrain height and results in darker areas in the SAR detected image, where no signal rather than the system noise floor is present. Layover, instead, happens when the terrain height increases in the line-of-sight direction. In this case multiple targets returns are received at the same slant range time resulting in an increased reflectivity. These two contributions interfere and cannot be separated unless multiple acquisition techniques are used. A visual example is presented in **Figure 2**.

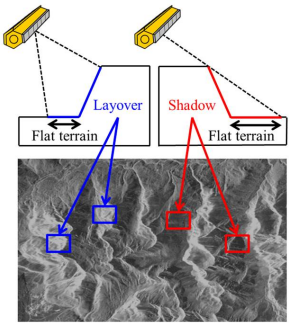

Figure 2: Shadow and Layover effects in a SAR image.

2.1 Detection Algorithm

The used shadow and layover detection algorithm is based on the work presented by *Kropatsch and Strobl* in [4]. They derived a mathematical formulation to detect Shadow and Layover areas, by analyzing all possible cases of interaction and superposition of the two phenomena.
With respect to [4], we kept the algorithm approach to independently generate the Shadow and Layover maps. Instead we modified the approach to solve the superposition of Shadow and Layover and merge the two masks in a single Shadow Layover Map (SLM). As in [4], we split Layover areas in two contributions: Active Layover and Passive Layover regions. Active Layover regions are sources which directly generate Layover, while Passive Layover regions are part of Layover just because the Active region lays upon them.
As presented in [4] we identify Active Layover regions with the equation:

$$R(d) = d - (z_s - z(d))\frac{\partial z(d)}{\partial d} \leq 0 \qquad (1)$$

Where d is the Euclidean distance between the sensor Nadir and the target Nadir, z_s is the sensor height, $z(d)$ is the target height, and $\frac{\partial z(d)}{\partial d}$ is the first derivative of the DEM range profile.
If we name the boundaries of an active layover region as B and C, we can define the boundaries of passive layover regions as:

$$r(A) = r(C) \qquad (2)$$

$$r(B) = r(D) \qquad (3)$$

Where $r(\cdot)$ is the slant range distance between the sensor and the target.

Thus obtaining the following Layover regions (as in **Figure 3**):

- from A to B: Passive Layover region
- from B to C: Active Layover region
- from C to D: Passive Layover region

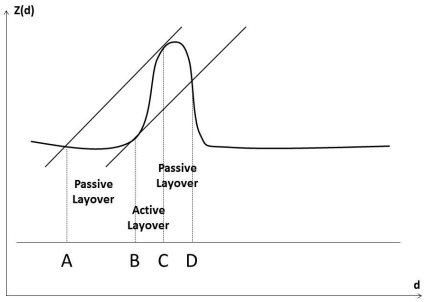

Figure 3: Layover geometry where it is highlighted the Layover region, subdivided in Active and Passive Layover.

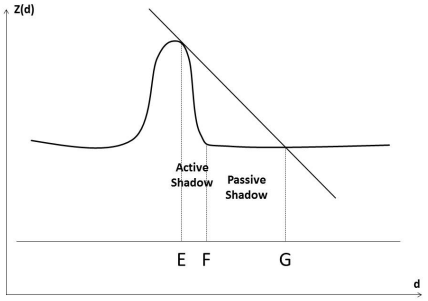

Figure 4: Shadow geometry where it is highlighted the Shadow region, subdivided in Active and Passive Shadow.

As in [4], we split Shadow areas into two contributions: Active Shadow and Passive Shadow regions.
Active Shadow regions are the direct sources of Shadow, while Passive Shadow regions are part of Shadow just because the Shadow region is projected over them.
Active Shadow regions can be identified with the equation:

$$R(d) = (z_s - z(d)) + d\frac{\partial z(d)}{\partial d} \leq 0 \qquad (4)$$

If we name the boundaries of Active Shadow region as E and F, we can define the boundaries of Passive Shadow regions as:

$$\alpha(G) = \alpha(E) \qquad (5)$$

Where $\alpha(\cdot)$ is the look angle between the sensor and the target.
Thus obtaining the following Shadow regions (as in **Figure 4**):

- from E to F: Active Shadow region
- from F to G: Passive Shadow region

Since we independently identify Shadow and Layover maps, a superposition of the two masks in some areas may occur. An example is presented in **Figure 5**: in this case, a relief, which is an active source of layover, is completely included in a shadow region, generated by the relief on the left-hand side.

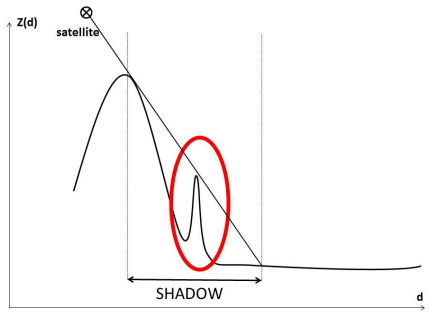

Figure 5: Example of an Active Layover area totally hidden by a Shadow region.

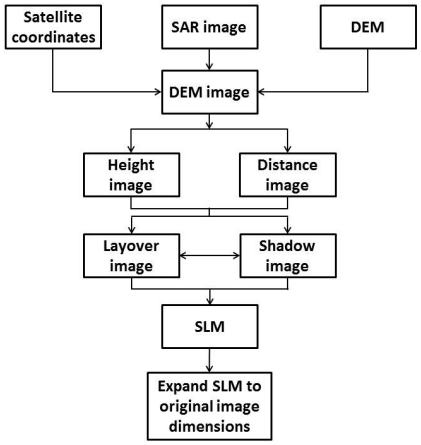

Figure 6: Algorithm workflow for the generation of a SLM image.

A layover contribution will therefore be present within the layover map but in reality this contribution is hidden by shadow. Therefore, rather than considering all cases presented in [4], we follow the criteria that Layover typically prevails over Shadow since if we have any contribution from Shadow and multiple contributions from Layover, the result will be the superimposition of Layover contributions. Only when the Active Layover region is completely bounded by a Shadow area, the Shadow prevails over Layover since the slope that would create Layover is not illuminated at all by any SAR signal. This choice allows us to correctly solve the ambiguity of areas that are mapped both as Shadow and Layover by the respective independent algorithms.
The complete workflow of the proposed algorithm is presented in **Figure 6**. The algorithm takes as input the SAR image, the geometry parameters, and the ancillary information of an external DEM. In this way it is possible to obtain the satellite georeferenced acquisition coordinates and resample the DEM over the SAR acquisition grid, obtaining the map indicated as DEM image. Applying the previously described algorithm we independently generate the Shadow and Layover images. In order to solve the Shadow and Layover interaction, at first we eliminate the Layover regions that are not illuminated by any SAR signal as they are shadowed by a Shadow region, then we superimpose the Shadow image and the Layover image as we previously described.
A visual example for a cutout of a TanDEM-X acquisition over the German Alps is presented in **Figure 7**, showing the SAR image amplitude on the left and the corresponding SLM on the right.

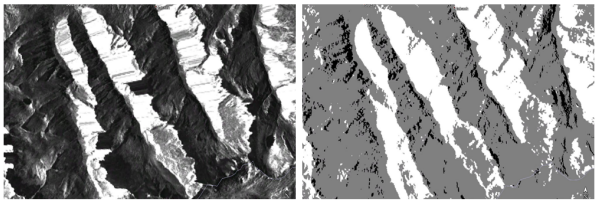

(a) (b)

Figure 7: (a) - Amplitude crop of a TanDEM-X acquisition over the Austrian Alps. (b) - corresponding SLM (Layover: white, Shadow: black).

3 Dataset and Test Site

For the current work, we chose a suitable test site where there is a consistent presence of both steep and flat terrain and diffuse water bodies. It is comprised between Longitude 12E and 13E, Latitude 47N and 48N and corresponds to a mountainous area over the Alps, between Austria and Germany. To obtain the coverage of the entire area, we used the complete set of 62 TanDEM-X images, which were used to generate the TanDEM-X DEM [1] over such an area and its WAM.
Additionally, the following data has been used:

- The SRTM DEM has been provided by [5].
- The slope map is derived by SRTM DEM [5].
- The Lidar DEM of Austria has been provided by [6].
- The water mask that we have used as external reference to validate both our results and the original TanDEM-X WAM results, has been provided by [7].

4 Water Masks Generation and Performance Analysis

In this section we present an analysis of the impact that different factors have on the accuracy of water detection. In particular, we quantify the impact of the proposed Shadow and Layover detection on the operational TanDEM-X WAM generation algorithm. We then asses the impact of the DEM accuracy itself, by comparing

maps generated using SRTM and Lidar DEMs, and, finally, we show an example of enhanced TanDEM-X WAM, with optimized threshold for the slope map filter, that leads to a significant quality improvement quality.
From now on, our WAM will be named EWAM (Enhanced WAM).
In order to asses the obtained performance, we consider the following accuracy index ACC, derived from the confusion matrix between each WAM and the external reference water mask as:

$$ACC = \frac{(TP + TN) - (FP + FN)}{TOT} \qquad (6)$$

Where TP is "True Positive", TN "True Negative", FP "False Positive", FN "False Negative", and TOT is the total number of pixels.

4.1 Impact of Shadow and Layover

In order to quantify the impact of applying a correct Shadow and Layover mask, we firstly implemented the same water detection algorithm as in [2] but substituted the Shadow/Layover mask provided by ITP with the newly derived SLM image for the initial filtering. SRTM DEM was used as reference input DEM. This approach allows us to perform a fair comparison between our proposed method and the already existing TanDEM-X WAM.
In order to keep the comparison as simple and clear as possible, we decided to consider the TanDEM-X WAM derived from the thresholding of the coherence values only (no amplitude is considered). We made this choice as the TanDEM-X WAM derived from the coherence thresholding, is generally performing better than the one derived from the thresholding of radar brightness, or from the joined thresholding of both quantities.
In both cases, we keep the same thresholding values:

- threshold at 0.23 for the coherence
- threshold at -18 dB for the radar brightness
- threshold at 20% for the slope map.

Then, a mosaicking strategy is applied in order to join and match all available overlapping acquisitions.
The last step consists in a post-processing to eliminate single pixels that may represent very small water bodies, or single pixels remained unfiltered by an improper Shadow/Layover or slope filtering.
Figure 8 shows a crop of the different confusion matrices between the WAM/EWAM and the external reference map. As it can be seen the EWAM, is much more precise than the already existing WAM, showing a total accuracy (evaluated on the entire tile of 1x1 degrees in lat/lon) of 0.972, with respect to the WAM, whose accuracy is 0.856.

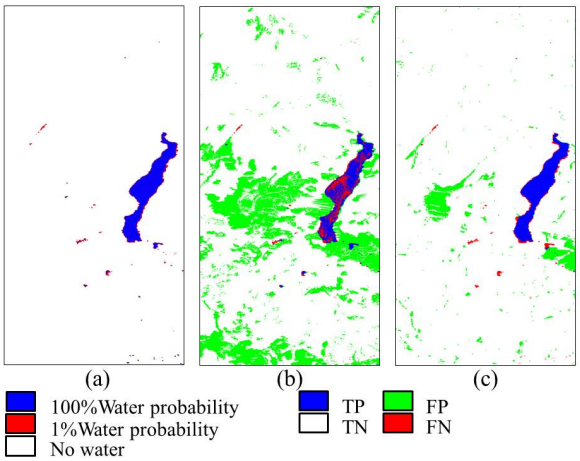

Figure 8: Confusion matrices between WAM/EWAM and the external reference in the surroundings of Koenigsee lake. (a) - Reference, (b) - WAM, (c) - EWAM SRTM (slope <20%). TP = "True Positive", TN = "True Negative", FP = "False Positive", FN = "False Negative".

4.2 Impact of the external DEM

The impact of the external reference DEM in the evaluation of the SLM image and, consequently, of the EWAM has been investigated by taking into account two different reference DEMs: namely SRTM and Lidar, introduced in section 3. As for the analysis in subsection 4.1, the corresponding confusion matrices of the same crop are visible in **Figure 9**. As expected, the EWAM computed with the Lidar DEM is more precise than SRTM, as it removes some errors related to very difficult areas characterized by strong topography, achieving an accuracy of 0.986.

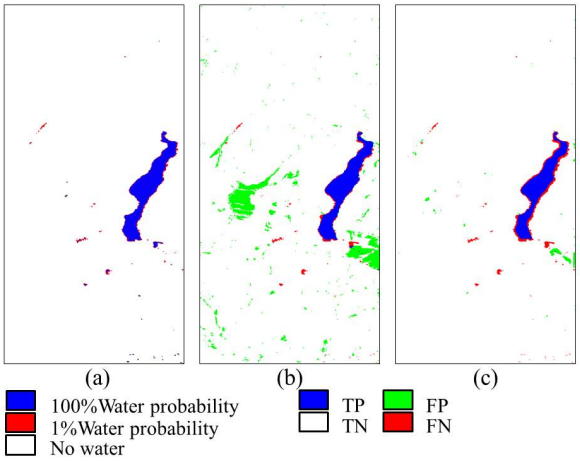

Figure 9: Confusion matrices between WAM/EWAM and the external reference in the surroundings of Koenigsee lake. (a) - Reference, (b) - EWAM SRTM (slope <20%), (c) - EWAM Lidar (slope <20%).

Nevertheless, it should be highlighted that, even with SRTM, the algorithm performs very well. This aspect is very encouraging, particularly if oriented toward the generation of a global product, for which Lidar DEMs could not be used at very large scale.

4.3 Impact of the Slope Threshold

As shown in the previous subsections, the EWAM, evaluated using the same thresholding as the WAM, already provides an improved performance with respect to the WAM itself. Nevertheless, a finer tuning of input parameters can lead to a further quality improvement: in particular, we investigate here how a proper slope thresholding can impact the final accuracy.
The original WAM thresholding is fixed at 20% slope, but this is a far too way conservative threshold.
From experimental analysis, a lower but still very conservative threshold can be set around 7%, assuring a better filtering of false detected water bodies. The obtained confusion matrices for two EWAM, generated using both slope thresholds, are shown in **Figure 10**. Reducing the threshold to 7% allows for a further improvement of the final accuracy of about 0.01%.

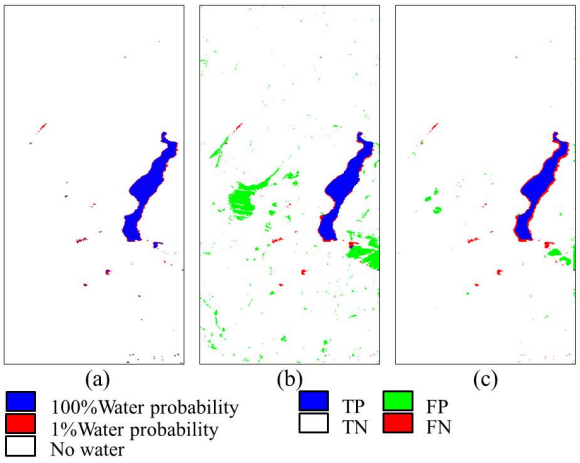

Figure 10: Confusion matrices between WAM/EWAM and the external reference in the surroundings of Koenigsee lake. (a) - Reference, (b) - EWAM SRTM (slope <20%), (c) - EWAM SRTM (slope <7%).

As summary, all evaluated accuracies for the analyzed cases are shown in **Table 1** and the corresponding confusion matrices for the complete tile are depicted in **Figure 11**. The EWAM, generated using SRTM and slope threshold at 7%, shows a very encouraging performance, which is comparable to the one obtained using the Lidar DEM with the same slope threshold. It is also observed that, when the quality of the DEM is higher (Lidar DEM), the algorithm performs at its best also with a higher slope threshold (20%).

Accuracy (ACC)		
Water Mask	slope <20%	slope <7%
WAM	0.856	-
EWAM SRTM	0.972	0.986
EWAM Lidar	0.986	0.986

Table 1: Summary of Water Masks accuracy, evaluated as in (6) for the entire tile.

Finally, in order to better appreciate its high-level of detail and accuracy, the EWAM SRTM (slope <7%) for the entire tile is depicted in **Figure 12**, together with two optical images from ©GoogleEarth over Chiemsee and Koenigsee lakes, which confirm the precise detection of such water bodies.

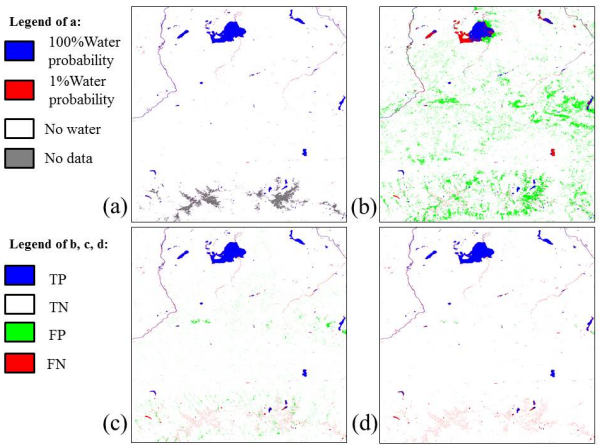

Figure 11: Confusion matrices between WAM/EWAM and the external reference for the entire tile of 1x1 degrees in lat/lon. (a) - Reference, (b) - WAM, (c) - EWAM SRTM (slope <20%), (d) - EWAM SRTM (slope <7%).

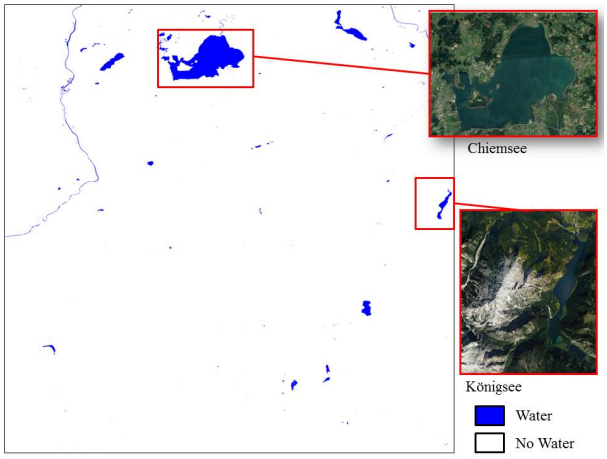

Figure 12: EWAM of the entire tile of 1x1 degrees in lat/lon, generated using SRTM DEM and setting the slope threshold at 7%. The two crops display two optical images from ©GoogleEarth over Chiemsee and Koenigsee lakes.

5 Conclusions and Outlook

In this paper, we proposed an effective approach for enhancing the existing TanDEM-X WAM. This work highlights the possibility of obtaining a more reliable water detection by simply improving the quality of the required inputs of the existing TanDEM-X WAM generation algorithm. In particular, the obtained results confirm that an accurate estimation of shadow and layover areas, together with a finer tuning of the algorithm settings, drastically improve the final performance over high-relief terrain.

The next step will consist in the development of a better algorithm for the detection and mosaicking of water bodies, aiming at generating large-scale mosaics with enhanced performance.

References

[1] G. Krieger, A. Moreira, H. Fiedler, I. Hajnsek, M. Werner, M. Younis, M. Zink: *"TanDEM-X": A satellite formation for High resolution SAR interferometry*, IEEE Transactions on Geoscience and Remote Sensing, vol. 45, n. 11, pp. 3317-2241, Nov. 2007

[2] A. Wendleder, B. Wessel, A. Roth, M. Breunig, K. Martin, S. Wagenbrenner: *TanDEM-X Water Indication Mask: Generation and First Evaluation Results*, IEEE Journal of Selected Topics in Applied Earth Observations and Remote Sensinf, vol. 6, n. 1, Feb. 2013

[3] Fritz T.; Rossi C.; Yague-Martinez N.; Rodriguez-Gonzalez F.; Lachaise M.; Breit H.: *Interferometric Processing of TanDEM-X data*, Geoscience and Remote Sensing Symposium (IGARSS) Proceedings, pp. 2428-2431, July 2011, Vancouver (Canada).

[4] W.G. Kropatsch, D. Strobl: *The Generation of SAR Layover and Shadow Maps From Digital Elevation Models*, IEEE Transactions on Geoscience and Remote Sensing, vol. 28, n. 1, pp. 98-107, Jan. 1990

[5] M. Kobrick, R. Crippen: NASA JPL. *NASA Shuttle Radar Topography Mission Global 1 arc second. 2013*, distributed by NASA EOSDIS Land Processes DAAC, `https://doi.org/10.5067/MEaSUREs/SRTM/SRTMGL1.003`

[6] Lidar Digital Terrain Model of Austria: `http://data.opendataportal.at/dataset/dtm-austria`, under the following Licence: Creative Commons Attribution 4.0 (CC BY 4.0)

[7] J.F. Pekel, A. Cottam, N. Gorelick, A.S. Belward: *High-resolution mapping of global surface water and its long-term changes*, Nature 540, 418-422 (2016). (doi:10.1038/nature20584)